The International Journal of Advanced Manufacturing Technology
https://doi.org/10.1007/s00170-026-17834-y

ORIGINAL ARTICLE

Hot deformation characteristics and constitutive modeling of Si-Doped γ-TiAl intermetallic alloy

John Jimmy M. Ellard[1] · Maria Ntsoaki. Mathabathe[2] · Charles Witness Siyasiya[3] · Amogelang Sylvester Bolokang[4]

Received: 19 November 2025 / Accepted: 2 March 2026

Abstract
Hot working remains a key approach for refining microstructures and enhancing the mechanical performance of γ-TiAl-based alloys. This study examines the hot deformation behavior of a Si-doped γ-TiAl intermetallic alloy with a nominal composition of Ti-48Al-2Nb-0.7Cr-0.3Si (at%). Uniaxial compression tests were conducted using a Gleeble 1500DTM thermomechanical simulator, over a temperature range of 1050–1200 °C and strain rates of 0.001-0.1 s^{-1}. The alloy was produced from cold-compacted precursor powders and consolidated through vacuum arc re-melting to ensure compositional uniformity. Prior to testing, the machined specimens were homogenized and polished to remove surface imperfections. The results indicated that the deformation response was predominantly characterized by the formation of macro-cracks associated with 45° shear localization across the specimen mid-section. Despite this a stable hot working window was identified between 1050 and 1080 °C and strain rates of 0.0087–0.071s^{-1}. The activation energy for hot deformation was calculated as 401 kJ/mol, and a constitutive equation was established to describe the flow stress behavior. Hot working within the optimal conditions resulted in refined grains with a mean grain size of 4 μm, as measured by EBSD, which exhibited improved elastic properties.

Keywords Hot deformation · Grain refinement · Constitutive equation · Intermetallic · γ-TiAl alloy

1 Introduction

The deformation of engineering materials especially metals can be done either at room temperature (cold-working) or at elevated temperatures (hot-working). However, extensive research has shown that a sound cold or warm deformation of γ-TiAl-based alloys is almost impossible as the alloys majorly consist of two ordered phases viz. α_2 (Ti_3Al) and γ (TiAl) [1]. The ordering in these phases decreases the capability of plastic deformation in the sense that only a few deformation modes are activated [2, 3] and the twinning and $c + a$ slip are rarely observed. Moreover, cross-slip is also inhibited as a result the stresses due to the dislocation density in the slip bands usually initiate cracking [2]. Although modifications can be made to the γ-TiAl-based alloys to increase their room temperature plasticity by alloying with elements such as Nb, Cr, and V [4, 5], , it has been proven that these adjustments are still insufficient to promote efficient workability even at temperatures as high as 900 °C. For instance, Kim et al., [6] reported that the hot-deformation of an alloy with a chemical composition of Ti-46Al-1.9Cr-3.0Nb-0.18 W-0.16B-0.13 C (at%) was accompanied by surface and intergranular cracking as well as flow localisations at temperatures lower than 900 °C. Even though the addition of these alloying elements stabilises the disordered body-centred cubic β-phase and promotes hot-workability [7, 8], the disordered β-phase transforms into the ordered β-phase as the temperature drops to 1175 °C [9]. The latter further ebbs the room-temperature plasticity [7, 8].

✉ Maria Ntsoaki. Mathabathe
maria.mathabathe@wits.ac.za

1 Department of Engineering, Malawi University of Science and Technology, Limbe MW310105, Malawi

2 School of Chemical and Metallurgical Engineering, University of the Witwatersrand, 1 Jorissen St, Private bag 3, 2050, Braamfontein, Johannesburg 2050, South Africa

3 Department of Material Science and Metallurgical Engineering, Faculty of Engineering, Built Environment and Information Technology, University of Pretoria, Pretoria, South Africa

4 Center for Nanoengineering and Advanced Materials, School of Mining, Metallurgical and Chemical Engineering, University of Johannesburg, Doornfontein, P.O. Box 17011, 2088 Johannesburg, South Africa

Published online: 17 March 2026

Therefore, the only possible window for efficient working with γ-TiAl-based alloys appears to be at elevated temperatures, usually above 900 °C.

However, the precise parameters in terms of strain rates and temperatures that define regions that allow the crack-free working of these alloys are majorly influenced by microstructure and alloy composition, especially the Al content [3]. The higher the Al concentration, the wider the crack-free working condition ranges [3]. Several hot-workability maps have been obtained from various γ-TiAl alloy systems fabricated through processes such as powder metallurgy (P/M) and ingot metallurgy (I/M) [6, 10–18]. Zhang et al., [10] investigated the hot-working behavior of a Ti-47Al -2Cr- 0.2Mo (at%) alloy produced by a plasma rotating electrode process (PREP) from an alloy powder. The researchers found that the dynamic recrystallization (DRX) of the alloy took place at a temperature and a strain rate of around 1000 °C and 10^{-3} s^{-1} respectively when the sample was deformed at a strain of 0.7. In another study done by Huang et al. [11], the hot compression behavior of a steel-canned Ti-45Al-7Nb-0.15B-0.4 W (mole fraction %) alloy was investigated using a Gleeble 1500 hot simulator. The experiments were conducted within the temperature range of 1050–1230 °C, and at a strain rate of $0.01s^{-1}$. They found that the hot compression of the alloy was safe between 1050 and 1230 °C, and the optimum temperature was found to be 1180 °C. Concerning the hot deformation of the second generation of γ-TiAl-based alloys, the so-called 48-2-2, Chen et al. [18] studied the DRX and established the hot-processing map of the alloy. In their study, the alloy produced by vacuum arc remelting (VAR) was compressed isothermally at temperatures of 1000, 1050, 1100, 1150 and 1200 °C, and strain rates of 0.001, 0.01, 0.05 and 0.1 with 60% height reduction. The researchers reported that the optimum thermo-mechanical treatment could be carried out on the alloy at either 1100 °C with a strain rate of $0.001s^{-1}$ or at 1200 °C with a strain rate of $0.01s^{-1}$. Recently, Hu et al., [19] studied the deformation and DRX nucleation mechanisms as well as the relationship between microscopic mechanism and efficiency of power dissipation in a Ti-48Al-2Nb-2Cr alloy with a near gamma microstructure fabricated by PREP from the pre-alloy powder. The researchers reported that the temperature and strain rate ranges suitable for highly efficient hot working for the alloy were 1180–1210 °C and 0.001–0.01 s^{-1} respectively. Furthermore, they elucidated that the softening mechanism for the alloy was primarily through DRX which was closely related to the disordered transformation of $\alpha_2 \rightarrow \alpha$. In addition, they observed that elevated temperatures and reduced strain rates promoted the occurrence of DRX in the lamellar structure.

However, in most of these hot compression studies, the TiAl alloy specimens were hot isostatically pressed (HIPed). This could lead to complex processes that could require special equipment, thus rendering the fabrication process less cost-effective [20]. In addition, these previous investigations, as noticed by Chen et al. [18], focused mainly on the hot-working behavior of the novel β-solidification and high Nb-containing TiAl alloys whose corresponding results may not be suitable for the modified peritectic TiAl alloy systems viz. Ti-48Al-2Nb-0.7Cr-0.3Si [21, 22]. Therefore, the hot-working behavior of an as-cast Si-doped modified second generation γ-TiAl intermetallic alloy of nominal composition Ti-48Al-2Nb-0.7Cr-0.3Si (at%) was investigated by hot isothermal uniaxial compression tests in this study. It is noteworthy that this alloy was found to possess good oxidation properties in the air [23, 24]. However, its hot-working behavior is not yet known. To obtain the alloy's optimum hot-working parameters, the power dissipation map approach was adopted [14, 25, 26].

2 Experimental work

2.1 Hot-compression testing

A 38 × 38 × 13 mm^3 button ingot of nominal composition Ti-48Al-2Nb-0.7Cr-0.3Si (at%) fabricated by vacuum arc remelting (VAR) from cold-pressed precursor powders [21, 27, 28] was cut by electric-discharge machining as shown in Fig. 1a to produce hot compression cylindrical specimens of 10 mm length and 6 mm diameter. To minimise micro-segregation owing to the non-equilibrium solidification conditions [29], the samples were homogenised at 1250 °C for 2 h with subsequent furnace cooling. The specimens' surfaces were then polished to get rid of surface irregularities prior to the testing. A Gleeble 1500D™ thermomechanical processing simulator was employed to conduct single pass hot isothermal uniaxial compression tests at temperatures of 1050, 1100 and 1200 °C, and at strain rates of 0.001, 0.01, and 0.1 s^{-1}. A schematic diagram of the experimental setup before deformation in the Gleeble simulator is illustrated in Fig. 1b. During the tests, the specimens were heated at the rate of 10 °C/s to the required temperature in the argon protected atmosphere, followed by soaking for 2 min with subsequent compression to a true strain of 0.5. After compression, the samples were immediately quenched by helium gas to retain the as-deformed microstructures. The optimum hot-working parameters of the alloy were determined using the power dissipation map approach [30–32]. Optimal condition was defined as a region exhibiting a high proportion of energy dissipated through beneficial metallurgical mechanisms, particularly DRX. This region, characterized by elevated power dissipation efficiency, was validated through microscopy, which revealed fine and more equiaxed grains.

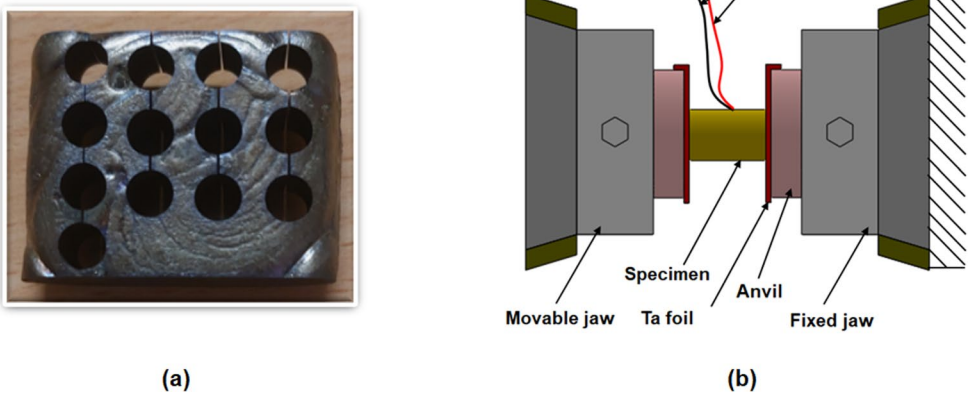

Fig. 1 (**a**) Electric-discharge machined button-ingot (**b**) Schematic representation of experimental setup before deformation

2.2 Microstructure characterization

The microstructures of the homogenized samples as well as the samples that successfully deformed without macro-cracks were characterized by a JEOL JSM-6510 scanning electron microscope (SEM) in a backscattered electron (BSE) mode and an Olympus BX51M reflected light microscope (LM). The specimens for the SEM and LM analysis were prepared by sectioning longitudinally with subsequent grinding and polishing mechanically to a mirror-like finish followed by etching in 24 ml H_2O + 50 ml glycerol + 24 ml HNO_3 + 2 ml HF solution [27, 33]. To identify the structural phases in the alloy, the X-ray diffraction (XRD) technique was employed. The parameters for XRD examination included: $\lambda = 1.54062$ Å and 2θ from 20° to 90° with a scan step size of 0.02° [34]. Additionally, SEM-EBSD was employed to characterize the grain sizes, texture intensities, misorientation angle distributions, elastic properties and dislocation densities of the samples that deformed without cracks. The samples were mechanically polished up to colloidal silica and subsequently electro-polished in a solution of 600 ml methanol, 360 ml butoxyethanol and 60 ml perchloric acid prior to the EBSD data acquisition. During the SEM-EBSD characterization, the acceleration voltage of 20 kV, the scanning interval of 0.4 µm, and the specimen tilted angle of 70° were used. The processing of the acquired EBSD data was carried out by AZtecCrystal software.

3 Results and discussion

3.1 Macro-analysis of the as-deformed specimens

The hot-deformation behavior of the alloy was macro-analyzed after the compression tests by visually inspecting the as-deformed samples. As can be seen in Fig. 2, the alloy's deformability was greatly influenced by the temperature and strain rate. At 1050 °C/0.1 s^{-1}, 1100 °C/0.001 s^{-1}, 1100 °C/0.01 s^{-1}, 1100 °C/0.1 s^{-1}, and 1200 °C/0.001 s^{-1}, the deformation was characterized by a 45° shearing of the mid portion of the specimen to form macro-cracks. This indicates that the alloy's hot workability was poor at these temperatures and strain rates. Fröbel and Stark [35] elucidated that during hot-working, shear bands and textures are formed owing to the plastic anisotropy of the γ-TiAl-based alloys. As the deformation strains are applied, the movement of dislocations responsible for the occurrence of deformation is low and the material tends to deform only in shear zones which are the local and narrow confined regions. Consequently, large volumes of the material remain nearly undeformed, and cracks nucleate and propagate within the shear bands [35]. A different scenario was observed at the temperature and strain rate of 1050 °C and 0.001 s^{-1} respectively, in which the sample wall bulged instead of shearing to form macro-cracks. Furthermore, at 1200 °C/ 0.01 s^{-1}, the specimen experienced both the bulging and shearing effects which led to the formation of cracks on the bulging surfaces. Moreover, while a large volume of the sample fully deformed, the bottom portion remained undeformed. However, the alloy exhibited good hot workability at the temperatures of 1050 °C when the strain rate was set to 0.01 s^{-1} as well as at the temperature and strain rate of 1200 °C and 0.1 s^{-1}, respectively. This was evidenced by the full bulging of the specimens' walls without the formation of cracks on their surfaces. Therefore, it could be inferred that the safe thermo-mechanical processing windows for the alloy are at 1050 °C with an intermediate deformation speed and at 1200 °C when the deformation speed is relatively high.

3.2 Deformation flow curves

Figure 3 exhibits the stress-strain curves obtained at different deformation temperatures and strain rates. In general,

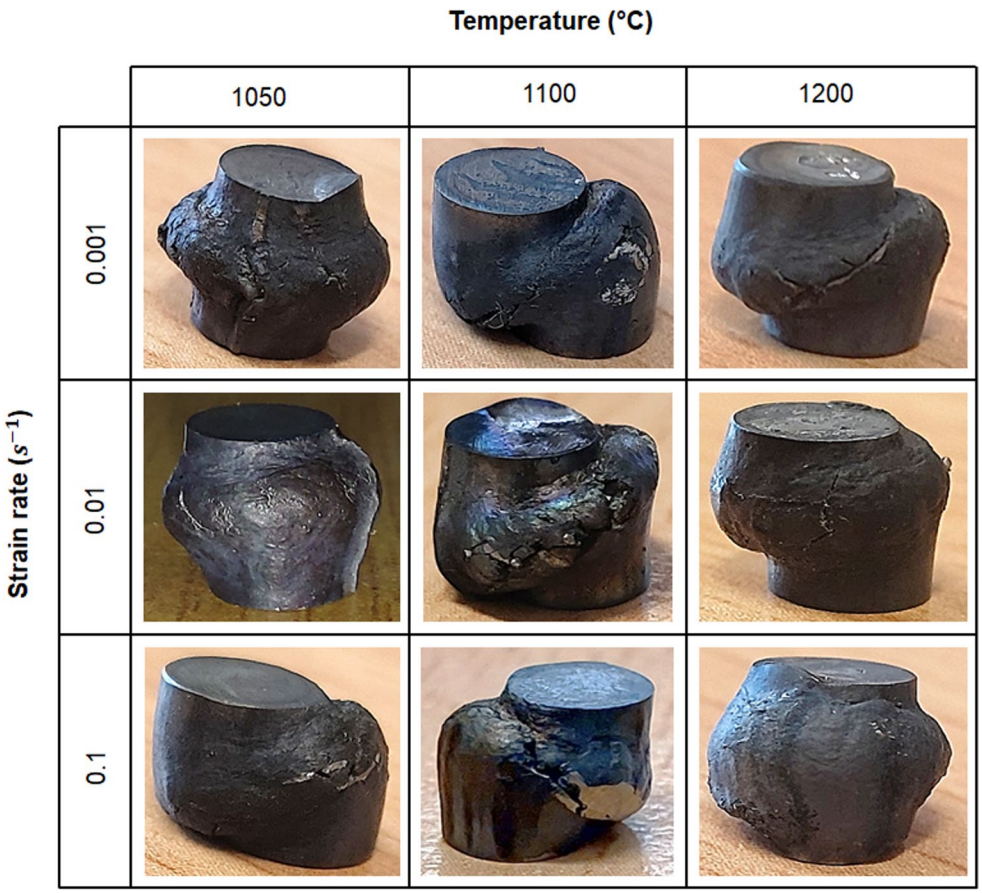

Fig. 2 Macroscopic morphologies of Gleeble compression simulated specimens as a function of strain rate and temperature at a true strain of 0.5

the flow curves display that the flow stress decreased significantly as the temperature increased and the strain rate decreased. The alloy which shows such flow behavior is classified as a low stacking-fault-energy (SFE) material [3, 36]. This material is characterized mainly by the decreased mobility of dislocations during a deformation process. Furthermore, as observed in Fig. 3, all the curves exhibited a dramatic increase in flow stress at the commencement of the compression tests until enough dislocations had piled up in the material. During this stage, the dislocation density increased in the alloy and subsequently, dislocation cells and subgrain boundaries were formed [37]. This was accompanied by the gradual hardening of the material which was observed to be sensitive to the magnitude of strain rate. At lower strain rates (i.e. 0.001 and 0.01 s^{-1}), the hardening occurred within a narrow range of strain at all the deformation temperatures whereas, at higher strain rates (i.e. 0.1 s^{-1}), it took place within a wide range of strain. In any case, the flow stress increased with increasing strain to reach the peak stress. The values of the peak stresses at different deformation temperatures and strain rates are shown in Table 1, and they demonstrate that the higher the deformation speeds, the higher the flow peak stresses (Fig. 4). After attaining the peak stress, a significant flow softening was initiated after dynamic recovery (DRV) had taken place as evidenced by the gradual decrease of flow stress with increasing strain at all temperatures. At this stage, the subgrains grew, and when the driving force reached a critical value, DRX occurred which led to the obliteration of dislocations and refinement of microstructure in the material [38]. Moreover, the progression of the flow softening process was also observed to depend on the speed of deformation. At strain rates of 0.01 and 0.1 s^{-1}, the softening in the samples continued until the set strain was attained while at 0.001 s^{-1}, the decreasing flow stress finally reached a steady-state value (σ_{ss}) at all tested temperatures when the equilibrium of work softening and work hardening was obtained [38] at a strain of about 0.4. This could suggest that DRX was maximized at this strain rate, which is beneficial for microstructure homogeneity.

3.3 Application of constitutive equations

Zener and Hollomon [38] proposed a temperature-compensated strain rate parameter, Z which is widely used to model the hot deformation behavior of a wide range of metals and alloys including γ-TiAl-based alloys under steady-state deformation conditions [39]. The parameter considers the

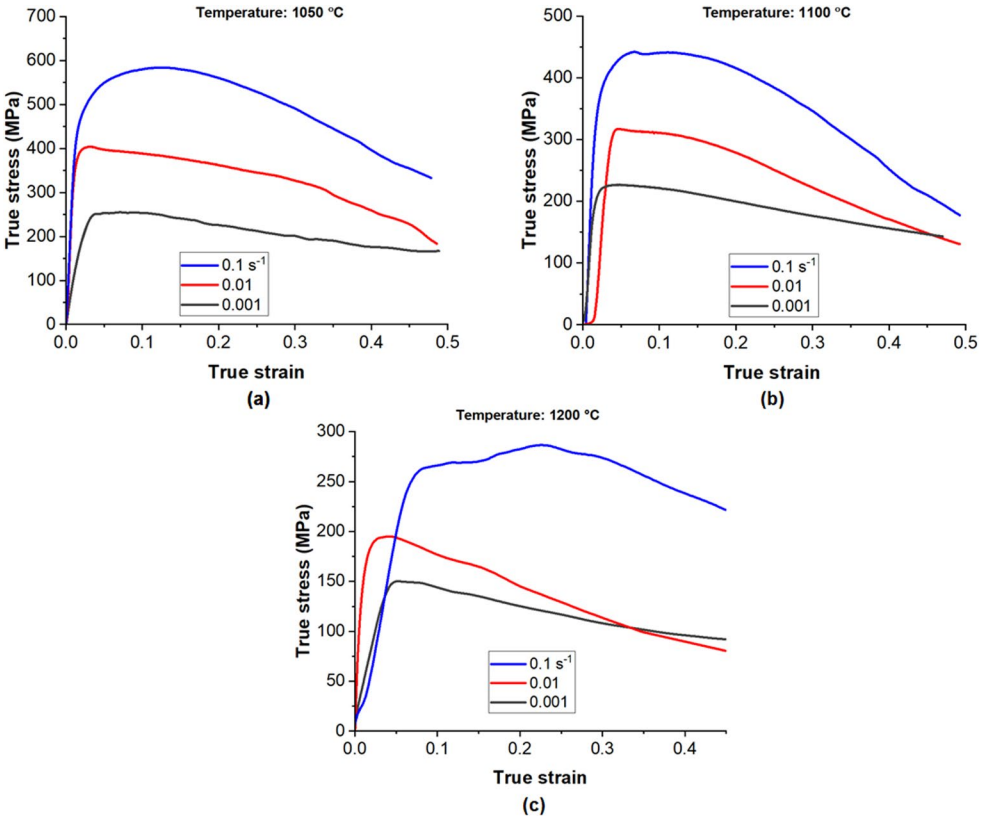

Fig. 3 Flow stress-strain curves of the alloy compressed at (**a**) 1050 °C, (**b**) 1100 °C and (**c**) 1200 °C

Table 1 Peak flow stress values as a function of temperature and strain rate at a true strain of 0.5

Temperature (T) (°C)	Strain rate ($\dot{\epsilon}$) (s^{-1})	Peak flow stress (σ_P) (MPa)
1050	0.001	263.89
	0.01	404.06
	0.1	584.40
1100	0.001	226.89
	0.01	317.28
	0.1	442.53
1200	0.001	150.05
	0.01	195.00
	0.1	286.47

deformation flow behavior of materials as a thermally activated process and relates the strain rate and the temperature as shown in Eq. (1).

$$Z = \dot{\epsilon}\exp\left(\frac{Q}{RT}\right) \tag{1}$$

where $\dot{\epsilon}$is the strain rate in s^{-1}, Q is the hot deformation's apparent activation energy in $J.mol^{-1}$, $R$is the universal gas constant which equates to 8.314 $J.mol^{-1}.K^{-1}$, and $T$is the temperature of deformation in K. It is noteworthy that Eq. (1) does not explicitly include the influence of flow stress which is one of the important variables in modelling the hot deformation behavior of a material. Therefore, Sellars and

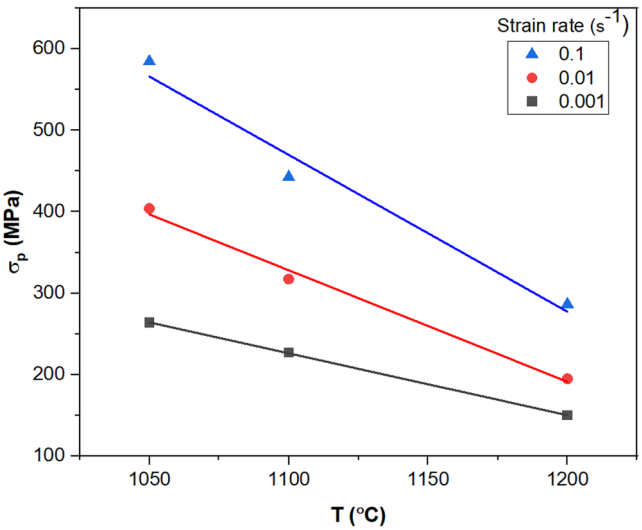

Fig. 4 Peak stress as a function of temperature and strain rate

McTegart [40] proposed a correlation for hot deformation data whose form is expressed in Eq. (2).

$$\dot{\epsilon}\exp\left(\frac{Q}{RT}\right) = A(\sinh\alpha\sigma)^n \tag{2}$$

where A, α and n are the material's constants independent of temperature: α is a parameter regulating the stress in MPa^{-1}, n is a stress exponent, and σ is the flow stress

in MPa. Equation (2) is known as the hyperbolic sinusoidal Arrhenius-type equation and is applicable for analysing hot deformation behavior across the entire stress range [41]. However, at low stresses (i.e. $\alpha\sigma < 0.8$) [42], Eq. (2) reduces to a power Arrhenius-type equation expressed in Eq. (3).

$$\dot{\epsilon}\exp\left(\frac{Q}{RT}\right) = A_1\sigma^{n_1} \tag{3}$$

where A_1 and n_1 are material's constants: n_1 is a stress exponent. Furthermore, at high stresses (i.e. $\alpha\sigma > 1.2$) [42], Eq. (2) reduces to an exponential Arrhenius-type equation expressed in Eq. (4).

$$\dot{\epsilon}\exp\left(\frac{Q}{RT}\right) = A_2\exp\beta\sigma \tag{4}$$

Where A_2 and β are material's constants. To determine the constants for the Arrhenius-type behavior of the alloy studied here, the data obtained from compression tests were employed. As observed from the flow curves exhibited in Fig. 3, the true stress values changed as the true strain increased, therefore, the correlation between the true stress and the material's constants was analysed at different values of the true stress. To obtain the value of α for the alloy in Eq. (2) for the entire stress range, the existing relationship between the material's constants at low and high stresses, and across the entire stress range shown in Eq. (5) was used.

$$\alpha = \frac{\beta}{n_1} \tag{5}$$

Rearranging Eqs. (3) and (4), and taking the natural logarithms of both sides of the equations, Eqs. (6) and (7) for low and high stresses respectively, were obtained.

$$\ln\dot{\epsilon} = \ln A_1 + n_1\ln\sigma - \frac{Q}{RT} \tag{6}$$

$$\ln\dot{\epsilon} = \ln A_2 + \beta\sigma - \frac{Q}{RT} \tag{7}$$

Using the strain rates and the peak stress data at different deformation temperatures, $\ln\dot{\epsilon} - \ln\sigma_p$ and $\ln\dot{\epsilon} - \sigma_p$ plots shown in Fig. 5 were obtained. As one could notice, the slope of $\ln\dot{\epsilon} - \ln\sigma_p$ plot in Fig. 5a represents the value of n_1 in Eq. (6) at each temperature whereas, the slope of $\ln\dot{\epsilon} - \sigma_p$ plot in Fig. 5b is equivalent to the value of β in Eq. (7) at each deformation temperature. Moreover, as can be seen in Fig. 5a, the slope variation between the deformation temperatures of 1200 and 1100 °C was almost negligible. Conversely, the variation of slope between the temperatures of 1100 and 1050 °C was more significant. Furthermore, in Fig. 5b, the slope decreased with decreasing deformation temperature. The average values of n_1 and β obtained from the linear fits to the data at 1050, 1100 and 1200 °C as well as the calculated value of α are shown in Table 2.

For the entire stress range, Eq. (2) was rearranged, and natural logarithms were taken at both sides of the equation to obtain Eq. (8).

$$\ln\dot{\epsilon} = \ln A + n\ln\left[\sinh\left(\alpha\sigma\right)\right] - \frac{Q}{RT} \tag{8}$$

Rearranging Eq. (8), Eq. (9) was yielded.

$$\ln\left[\sinh\left(\alpha\sigma\right)\right] = \frac{\ln\dot{\epsilon}}{n} + \frac{Q}{nRT} - \frac{\ln A}{n} \tag{9}$$

Now, taking partial derivatives of Eq. (9), the following Eq. (10) was derived for the activation energy.

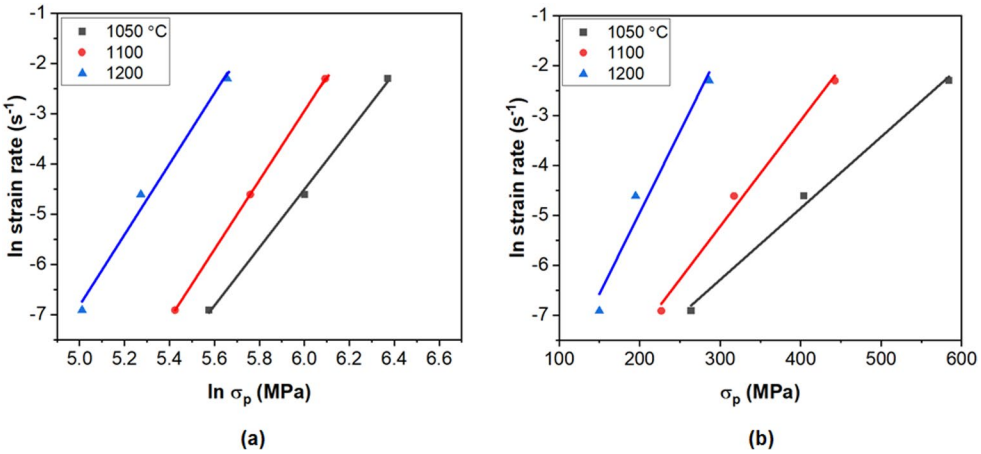

Fig. 5 Relationships between (**a**) $\ln\dot{\epsilon}$ and $\ln\sigma_p$, (**b**) $\ln\dot{\epsilon}$ and σ_p as a function of temperature

Table 2 Material's constants at temperatures of 1050, 1100 and 1200 °C, and strain rates of 0.001, 0.01, and 0.1 s^{-1}

Material's constant	Value
n_1	6.5709
β	0.0227
α	0.0035 MPa^{-1}
n	4.3205
A	3.0528 $\times 10^{13} s^{-1}$

$$Q = R\left\{\frac{\partial \ln \dot{\epsilon}}{\partial \ln\left[\sinh\left(\alpha\sigma\right)\right]}\right\}_T \left\{\frac{\partial \ln\left[\sinh\left(\alpha\sigma\right)\right]}{\partial\left(1/T\right)}\right\}_{\dot{\epsilon}} \tag{10}$$

The hot deformation data at different temperatures and strain rates were used to obtain the $\ln\dot{\epsilon} - \ln\left[\sinh\left(\alpha\sigma_p\right)\right]$ and $\ln\left[\sinh\left(\alpha\sigma_p\right)\right] - 1/T$ plots as depicted in Fig. 6. According to Eqs. (8) and (9), the value for n was the average value of the slopes of $\ln\dot{\epsilon} - \ln\left[\sinh\left(\alpha\sigma\right)\right]$ plots (Fig. 6a) at different temperatures expressed in Eqs. (11),

$$n = \frac{\partial \ln \dot{\epsilon}}{\partial \ln\left[\sinh\left(\alpha\sigma\right)\right]} \tag{11}$$

whereas, the value for Q/nR in Eq. (9) was the average value of the slopes of $\ln\left[\sinh\left(\alpha\sigma\right)\right] - 1/T$ plots (Fig. 6b) at different strain rates expressed in Eq. (12).

$$\frac{Q}{nR} = \frac{\partial \ln\left[\sinh\left(\alpha\sigma\right)\right]}{\partial\left(1/T\right)} \tag{12}$$

One could note that the right-hand side (RHS) terms in Eqs. (11) and (12) are similar to the multiplicand and multiplier at the RHS of Eq. (10). Therefore, the value for the activation energy (Q) for the alloy was calculated using the mean values of the slopes of $\ln\dot{\epsilon} - \ln\left[\sinh\left(\alpha\sigma_p\right)\right]$ and $\ln\left[\sinh\left(\alpha\sigma_p\right)\right] - 1/T$ plots. The mean value of n obtained from the linear fits to the data at 1050, 1100 and 1200 °C (Fig. 6a) is indicated in Table 2. Furthermore, the mean value of $\frac{Q}{nR}$ obtained from plots shown in Fig. 6b at strain rates of 0.001, 0.01 and 0.1 s^{-1} was 11.2269 K. The calculated value of Q was 401 $kJ.mol^{-1}$. Since the Zener-Hollomon parameter (Z) can also be related to the flow stress as expressed in Eqs. (13),

$$Z = A(\sinh\alpha\sigma)^n \tag{13}$$

the value for the material's constant, A indicated in Table 2 was obtained by using the intercept of $\ln Z - \ln\left[\sinh\left(\alpha\sigma_p\right)\right]$ linear fit plot shown in Fig. 6c.

The alloy's apparent activation energy for hot-working estimated in this study was compared with the ones for other γ-TiAl-based alloy systems found in the literature

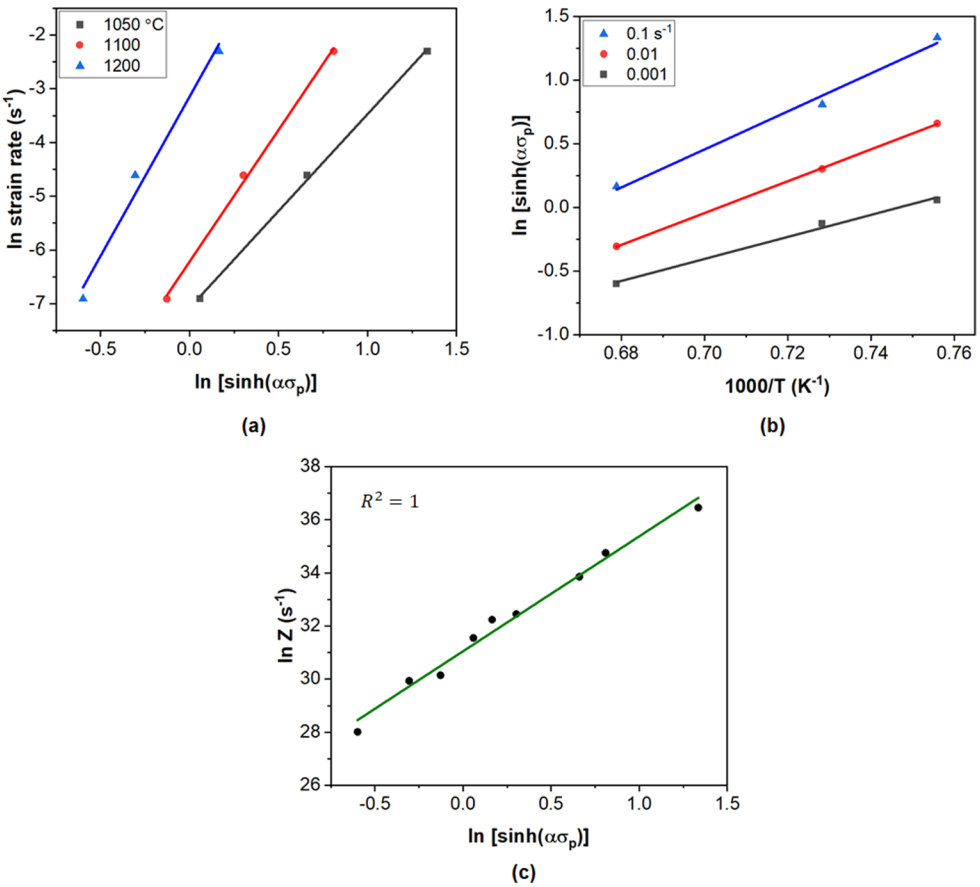

Fig. 6 Relationships between (**a**) $\ln\dot{\epsilon}$ and $\ln\left[\sinh\left(\alpha\sigma_p\right)\right]$ as a function of temperature, (**b**) $\ln\left[\sinh\left(\alpha\sigma_p\right)\right]$ and $1/T$ as a function of strain rate, and (**c**) $\ln Z$ and $\ln\left[\sinh\left(\alpha\sigma_p\right)\right]$ as a function of both temperature and strain rate

as illustrated in Table 3. So far, the lowest and highest published values of Q for γ-TiAl alloys are 267 and 600 kJ/mol, respectively. In general, the alloy with a lower value of Q ensures easier mobility of dislocation during hot-working, leading to better deformability [19]. Despite the determined Q value in the present alloy is moderate, it is still significantly higher than the activation energies of Ti-Al inter-diffusion, Ti and Al self-diffusions in single-phase γ-TiAl intermetallic alloys whose values are 295, 260 and 360 kJ/mol [43, 44] respectively. This implies that the deformation processes that are assisted by diffusion were hindered in the alloy. Furthermore, the incorporation of Si into the γ-TiAl-based alloy promoted the formation of stable silicide precipitates (Ti_5Si_3), which impeded dislocation motion and grain boundary sliding [45], thereby increasing the alloy's hot deformation activation energy.

$$\dot{\epsilon} = 3.0528 \times 10^{13}[\sinh(0.0035\sigma_P)]^{4.3205}\exp\left(-\frac{401000}{RT}\right) \quad (14)$$

The accuracy of this model is shown in Fig. 7 by good linear correlation. The coefficient of determination was 0.98, indicating a 98% prediction of the relationship between flow stress, strain rate and temperature.

3.4 High-temperature power dissipation map

Characterization of the hot working behavior of alloys can be conducted by several models viz. atomistic, kinetic and dynamic materials models [25]. However, out of these models, and for multi-phase alloys, the dynamic materials model (DMM) produces extensively used processing maps for guiding the hot-working process. To generate the power dissipation map in this study, the sample being deformed was regarded as a power dissipator. The sum of power (P) instantaneously dissipated in the form of thermal and crystal defects distortion energies is expressed in Eq. (15) [25].

$$P = \int_0^{\dot{\epsilon}} \sigma d\dot{\epsilon} + \int_0^{\sigma} \dot{\epsilon} d\sigma = G + J \quad (15)$$

where σ is the flow stress, $\dot{\epsilon}$ is the strain rate, G is the content representing deformation heat and J is the co-content representing microstructural dissipation. In an ideal situation, the power dissipated by the deformed material through microstructural changes, J reaches a maximum value and is expressed as:

$$J_{max} = \frac{1}{2}\sigma\dot{\epsilon} \quad (16)$$

Table 3 Apparent activation energies (Q) for hot-working of γ-TiAl-based alloys prepared by several processing routes

γ-TiAl alloy (at%)	Processing route	Temperature range (°C)	Q (kJ/mol)	Reference
Ti-48Al-2Nb-2Cr	PREP + HIP	1100–1250	371	[20]
Ti-48Al-2Nb-2Cr -0.2 W-0.1B	P/M + HIP	950–1250	315	[46]
Ti-48Al-2Nb-2Cr	Sintering + HIP	750–1250	387	[47]
Ti-46Al-4Nb-2Cr -2Mn	HIP of elemental powder	850–1050	387	[12]
Ti-45Al-8Nb-2Cr -2Mn-0.2Y	Cast + VLM	1000–1200	463	[43]
Ti-45Al-8Nb	As-cast	1000–1200	554	[16]
Ti-44Al-4Nb-1.0Mo-0.1B-0.01Y	Cast + HIP	1120–1240	525	[15]
Ti-43Al-3.59Nb-1Mo-0.16B	VAR + HIP	850–1050	267	[38]
Ti-42Al-6Nb-3Nb-0.1B	VAR + Forging	850–1100	424	[18]
Ti-45Al-5.4 V-3.6Nb-0.3Y	ISM + HIP	1100–1200	402	[48]
Ti-47Al-2Cr-0.2Si	Cast + HIP	1000–1100	260	[49]
Ti-48Al-2Nb-2Cr	P/M + HIP	1010–1260	385	[50]
Ti-46Al-8.5Nb-0.2 W	As-cast	900–1100	353	[51]
Ti-45Al-7Nb-0.4 W	Reaction sintering	1000–1200	420	[52]
Ti-43.9Al-4.3Nb-0.9Mo-0.1B-0.4Si	VLM + HIP	1100–1250	540	[53]
Ti-43Al-4Nb-1.4 W-0.6B	As-cast	1050–1200	580	[54]
Ti-43Al-9 V	Cast + HIP	1100–1200	577	[55]
Ti-43Al-9 V-0.3Y	Cast + HIP	1100–1200	451	[55]
Ti-45Al-5Nb	Cast + HIP	1100–1200	449	[55]
Ti-45Al-5Nb-0.3Y	Cast + HIP	1100–1200	400	[55]
Ti-43Al-4.1Nb-1.01Mo-0.11B	VAR + HIP	1150–1300	600	[17]
Ti-48Al-2Nb-0.7Cr-0.3Si	As-cast	1050–1200	401	This study

VLM Vacuum levitation melting, *ISM* Induction skull melting

Consequently, by substituting the measured Q value and the determined values of all the material's constants in Eq. (2), the constitutive equation for hot deformation of the alloy in a cast + homogenised condition expressed by hyperbolic sinusoidal function could be written as:

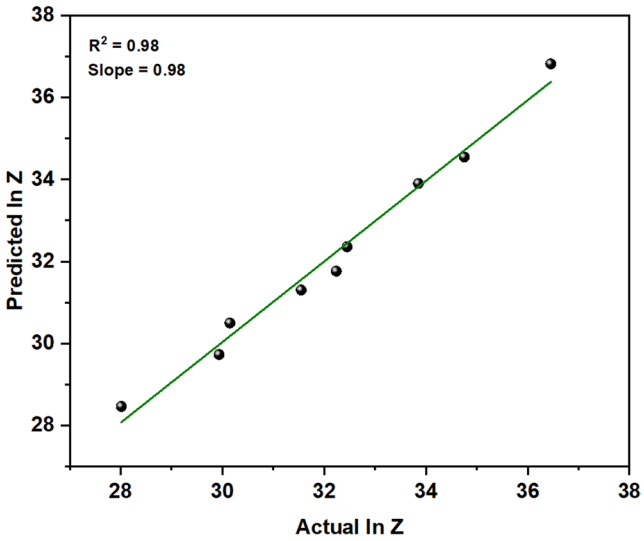

Fig. 7 Predicted versus actual values of Z

However, in practice, the value of J varies nonlinearly as the deformation conditions are varied. Therefore, the efficiency (η) of J-power dissipation is defined as [20]:

$$= \frac{J}{J_{max}} = \frac{2}{\sigma\dot{\epsilon}}\int_0^{\sigma}\dot{\epsilon}d\sigma \tag{17}$$

To define a constitutive relation for hot plastic deformation of the alloy, the widely used power law expressed in Eq. (18) is employed for constant strain and temperature.

$$\sigma = k\dot{\epsilon}^m \tag{18}$$

where k is a constant, and m is the strain rate sensitivity index. The nonlinear value of $m$can be expressed as:

$$m = \frac{dJ}{dG} = \frac{\dot{\epsilon}d\sigma}{\sigma d\dot{\epsilon}} \approx \frac{dlog\sigma}{dlog\dot{\epsilon}} \tag{19}$$

Therefore, combining Eqs. (17), (18) and (19), η can be expressed as [20]:

$$= \frac{2m}{1+m} \tag{20}$$

The values of m at different deformation temperatures and strain rates were determined using Eq. (19), and the power dissipation efficiencies were subsequently calculated using Eq. (20). The power dissipation efficiencies were then fitted with cubic splines to obtain an interpolated data array which was used to plot a power dissipation map.

Figure 8 displays the resulting power dissipation map. The map's contours depict iso-efficiency lines of power dissipation, which are directly proportional to the relative rate of entropy production in the system due to microstructure evolution. As illustrated in Fig. 8, the dissipation efficiency decreases with decreasing strain rate over the experimentally employed temperature range in the lower strain rate regime. On the other hand, the highest efficiency of about 32% can be achieved at approximately 1050 °C/0.024 s^{-1}, which may correlate with the optimum parameters for the hot working of this material. It is important to note that these optimum conditions are very close to one of the sets of parameters which was employed in this study (i.e. 1050 °C/0.01 s^{-1}). In general, two 'safe' regimes labelled 'S' were identified based on the values of η and crack-free deformation. As demonstrated in Fig. 8, one safe domain is located at the temperature range of 1050–1088°C and strain rate range of 0.0087–0.071s^{-1} whereas the other is located at higher temperatures and strain rates although not well defined. These results concur with the macro-analysis results of the deformed samples discussed in subsection 3.1 in which a satisfactory hot-workability for the alloy was observed to occur in samples deformed at temperatures of 1050 and 1200°C and strain rates of 0.01 and 0.1s^{-1}, respectively.

The optimum parameters for safe hot-working of γ-TiAl-based alloys are compared in Table 4. Although microstructural optimization in HIPed elemental powder can occur at the lowest deformation temperature of 950 °C, the deformation speed of 0.0001s^{-1} is rather low and therefore, it is difficult to achieve using conventional deformation equipment. Conversely, the alloy in this study exhibits the best combination of optimum parameters for hot working using conventional methods.

3.5 Analysis of microstructures

The microstructures of the as-homogenized and deformed samples are displayed in Fig. 9a-c. It is important to note that only the microstructures of the samples that were hot-compressed without the formation of cracks were analyzed. In both conditions (before and after deformation), the structures represented the characteristics of duplex microstructures consisting of γ grains (light grey contrast), and α_2/γ lamellar colonies (dark grey contrast). Furthermore, as exhibited by the X-ray diffraction pattern in Fig. 9d, the titanium silicate (Ti_5Si_3) precipitates were also formed owing to the addition of Si [59]. Before deformation, the microstructure comprised large grains (Fig. 9a) of the magnitude of about 400 µm. However, a significant grain refinement was induced in the microstructures during hot deformation. As can be observed in Fig. 9b, compressing the alloy at 1050 °C/0.01 s^{-1} resulted in the attainment of more equiaxed grains. Moreover, the sizes of the grains were reduced to the range of 3–15 µm. When the alloy was deformed at 1200

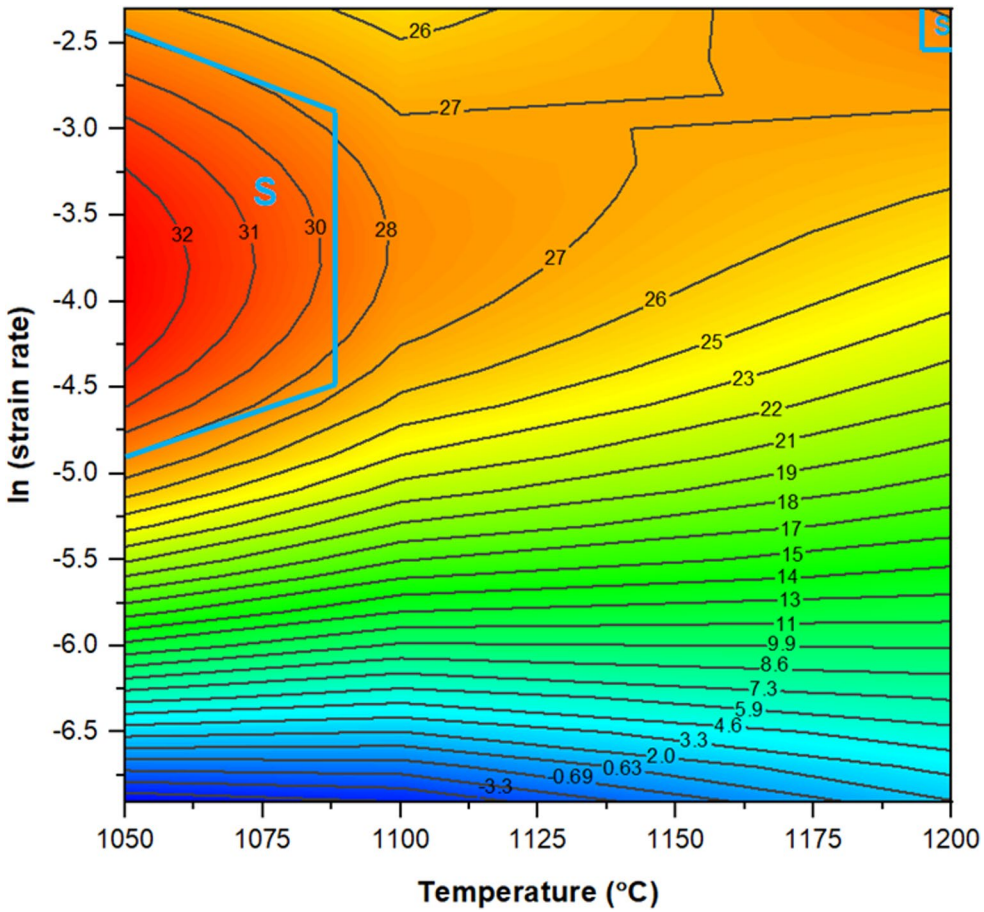

Fig. 8 Power dissipation map at a strain of 0.5. The efficiency of power dissipation in percentage is represented by the numbers along the contours

Table 4 Optimum parameters for safe hot-working of γ-TiAl-based alloys at various true strains

γ-TiAl alloy (at%)	Processing route	Strain	Optimum temperature (°C)/strain rate (s^{-1})	Ref.
Ti-48Al-2Nb-2Cr	Sintering + HIP	0.3	1100/0.001	[48]
Ti-45Al-7Nb-0.15B-0.4 W	Cast + HIP	0.3	1180/0.01	[11]
Ti-46Al-4Nb-2Cr -2Mn	HIP of elemental powder	0.5	950/0.0001	[12]
Ti-45Al-8Nb-2Cr-0.2B	As-cast	0.4	1100/0.005	[56]
Ti-42Al-6Nb-3Nb-0.1B	Cast + Forging	0.2, 0.4, 0.6	1100/0.001	[17]
Ti-43Al-4.1Nb-1.01Mo-0.11B	Cast + HIP	0.2	1250/0.05	[57]
Ti-48Al-2Nb-2Cr	Cast + HIP	0.92	1100/0.001 and 1200/0.01	[58]
Ti-48Al-2Nb-0.7Cr-0.3Si	As-cast	0.5	1050/0.0143	This study

°C/0.1 s^{-1} (Fig. 9c), an obvious grain refinement occurred. Nevertheless, the grains appeared to elongate perpendicular to the direction of the applied compressive load, which is consistent with the findings of Chen et al. [58] during the hot deformation of the 48-2-2 alloy.

The mechanism for grain refinement during thermo-mechanical processing of γ-TiAl-based alloys has been studied by several researchers [19, 20, 48]. All of them attest to the fact that the alloys undergo significant changes during hot deformation, and DRX is a crucial factor in this process. DRX mechanisms in high η regions are often categorised into discontinuous (DDRX) and continuous (CDRX) [19]. During hot deformation, the grain boundaries bulge and migrate, and with the accumulation of dislocations, DDRX grains nucleate along the grain boundaries to decrease the large dislocation gradient and high stored strain energy [60]. Furthermore, the lamellae colonies are kinked as shown in Fig. 10 and experience severe localised strain. This leads to the decomposition of the lamellar laths and nucleation of secondary DDRX grains [61]. It is noteworthy that since DDRX is not accompanied by the local lattice rotation in a single grain, the preferred orientation and the strong crystal texture are generally not achieved by the mechanism. On the other hand, CDRX usually occurs in the grain interior. As the strain increases, the dislocations continue to pile up, and due to dislocation climbing and rearrangement, sub-grain

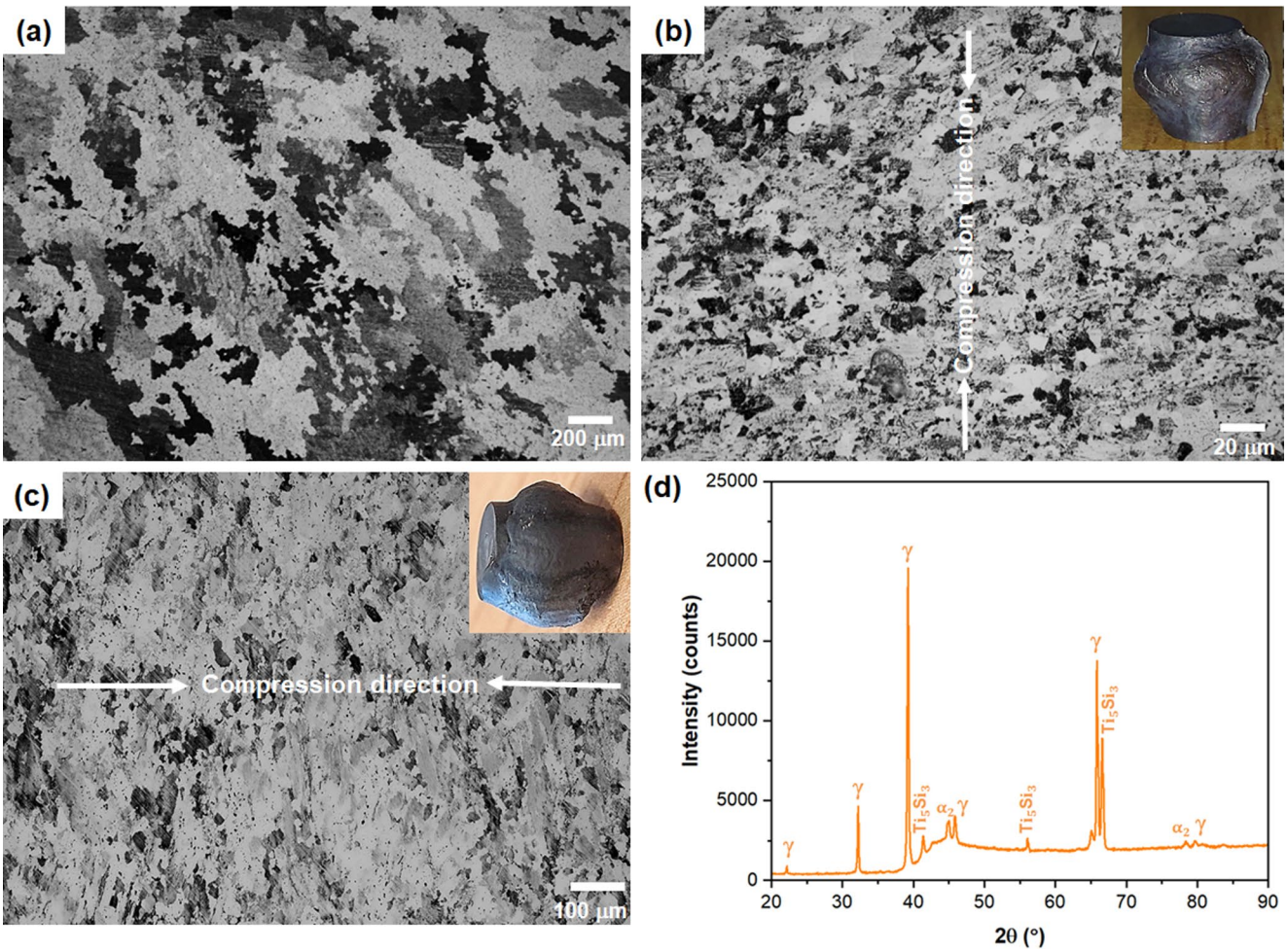

Fig. 9 (**a**) Initial microstructure of the alloy (**b**) microstructure of the sample deformed at 1050 °C/0.01s^{-1} (**c**) microstructure of the sample deformed at 1200 °C/0.1s^{-1} (**d**) XRD pattern of the alloy

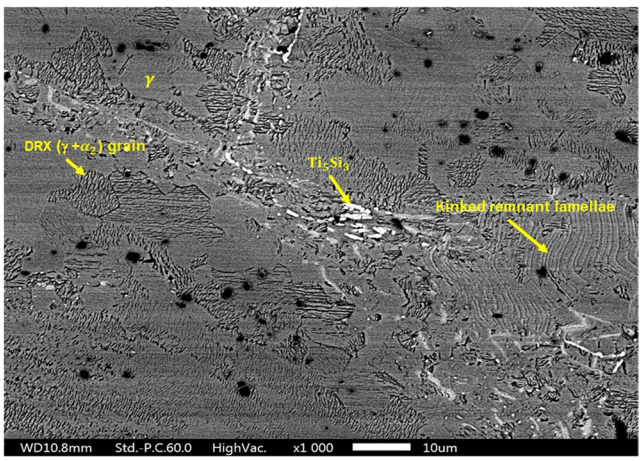

Fig. 10 SEM-BSE micrograph of the deformed alloy

boundaries form inside the deformed grains. With a further increase in strain, the sub-grain boundaries continue to absorb dislocations, leading to an increase in sub-grain misorientation and rotation [60]. Subsequently, the sub-grains become separate refined grains owing to the gradual transformation of low-angle grain boundaries (LAGBs) into high-angle grain boundaries (HAGBs). Unlike the DDRX mechanism, the CDRX ultimately changes the grain orientation and results in the emergency of orientation gradients in the microstructure.

As observed in Fig. 10, the deformed microstructure consisted of kinked remnant lamellae in addition to the DRX γ grains and DRX α_2/γ lamellar colonies. This concurs with the results of a previous study [56] which demonstrated that the thermo-mechanical processing at high temperatures does not completely break down the initial lamellar microstructures. It is speculated that the uneven dynamic recrystallization that occurs during hot deformation is due to the anisotropic plastic characteristics of lamellar colonies [56]. Apart from the microstructural constituents, elongated Ti_5Si_3 precipitates were also observed in the microstructure.

The majority of the precipitates aligned themselves in a chain-like structure as illustrated in Fig. 10. Sun and Froes [62] reported that the Ti_5Si_3 precipitates prefer to nucleate on the extended nodes or dislocation networks of $[10\ \bar{1}]$ superdislocations, where stacking faults exist.

SEM-EBSD maps are displayed in Fig. 11 in which (a) and (b) are phase maps, (c) and (d) orientation maps indicating inverse pole figures (IPF) in the x-axis for specimens deformed at 1050 °C/0.01 s^{-1} and 1200 °C/0.1 s^{-1}, respectively. The results demonstrate that the microstructures of both samples were dominated by the γ-TiAl phase with phase fractions of 90.5% for the former and 90.6% for the later specimens as indicated in Table 5. Apart from the γ-TiAl phase, the α_2-Ti_3Al phase and traces of Ti_5Si_3 precipitates with phase fractions of 5.82% and 3.49%, respectively, for sample deformed at 1050 °C/0.01 s^{-1} and 5.09% and 2.97% for sample deformed at 1200 °C/0.1 s^{-1} were also detected. The results concur with the ones obtained by SEM-BSE and XRD techniques elucidated earlier in this subsection. Furthermore, as can be observed in Fig. 11(a, b), the α_2 and Ti_5Si_3 phases were distributed almost evenly in the matrices of both samples.

Figure 12 exhibits the SEM-EBSD analysis of grain sizes for the specimens deformed at 1050 °C/0.01 s^{-1} (Fig. 12a, b) and 1200 °C/0.1 s^{-1} (Fig. 12c, d), in which (a) and (c) are all Euler color maps whereas (b) and (d) are histograms of the equivalent circle diameter grain size distribution. As can be seen, the grain sizes of the sample deformed at 1050 °C/0.01 s^{-1} predominantly ranged from 3.5 to 5.5 μm with an average of 4 μm. On the other hand, the substantial grain size range of 2.5–12.5 μm with a mean of 8 μm was exhibited by the sample deformed at 1200 °C/0.1 s^{-1}. It is evident that a finer and more equiaxed microstructure was obtained at the optimum hot-working parameters of 1050 °C/0.01 s^{-1}. The results further confirm the observation made in Fig. 9.

The textural intensities of the microstructural constituents are presented in Fig. 13 in terms of < 111 > inverse pole figures (IPF) for the specimens deformed at 1050 °C/0.01 s^{-1} (Fig. 13a, c,e) and 1200 °C/0.1 s^{-1} (Fig. 13b,

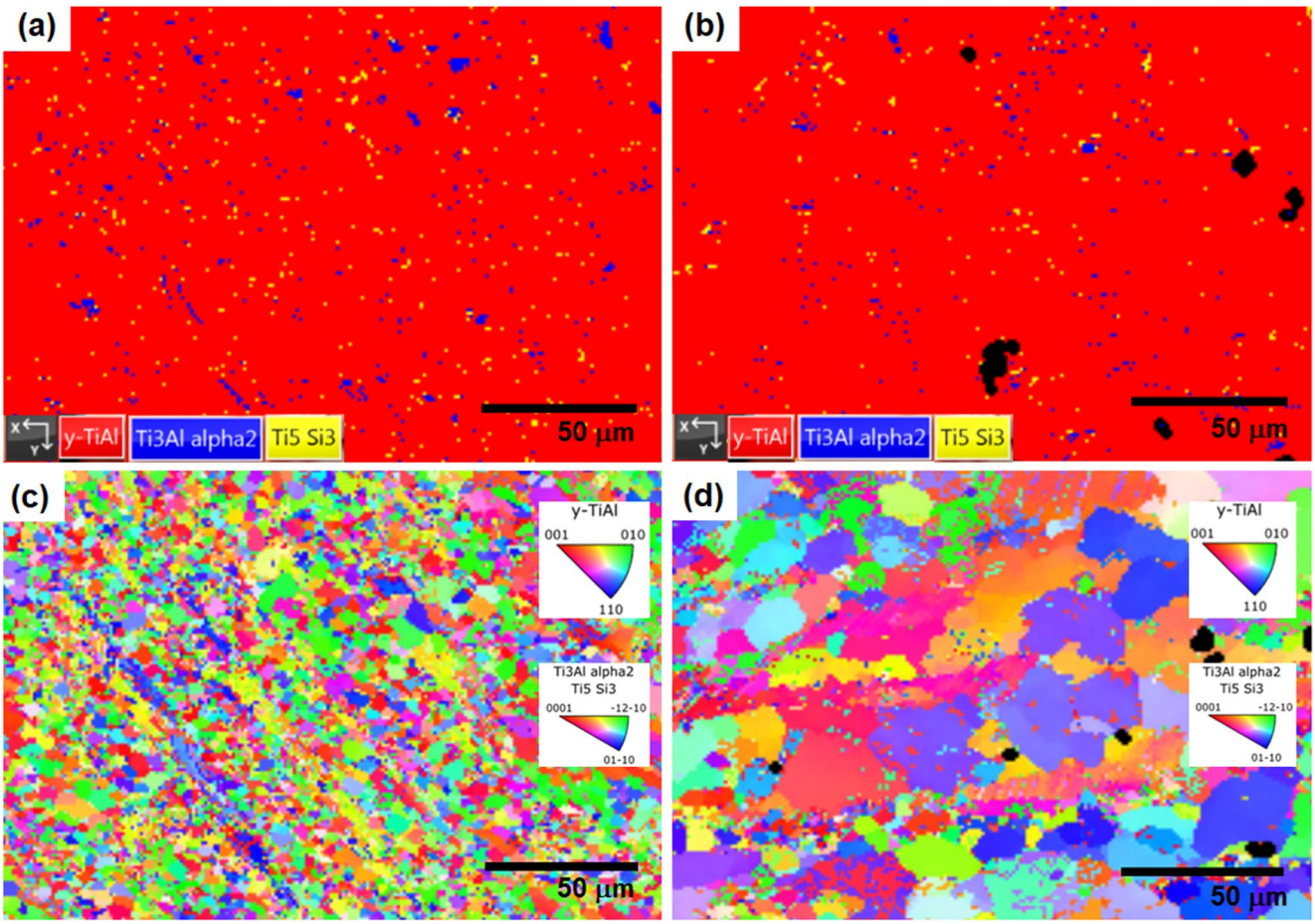

Fig. 11 EBSD maps: (**a**) and (**b**) phase maps, (**c**) and (**d**) orientation maps indicating inverse pole figure (IPF) in the x-axis of the samples deformed at 1050 °C/0.01 s^{-1} and 1200 °C/0.1 s^{-1}, respectively

Table 5 Phase fraction (%) acquisition

Phase name	Sample deformed at 1050 °C/0.01 s^{-1}	Sample deformed at 1200 °C/0.1 s^{-1}
Gamma (γ-TiAl)	90.5	90.6
Alpha 2 (α_2-Ti_3Al)	5.82	5.09
Ti_5Si_3	3.49	2.97

d,f). One could note that much weak orientation intensity was obtained in the sample deformed at 1050 °C/0.01 s^{-1} with maximum values of 1.99, 5.59 and 1.98 times stronger than a random distribution for γ-TiAl, α_2-Ti_3Al and Ti_5Si_3 phases, respectively. Conversely, high maximum values of 5.18, 8.51 and 3.05 for γ-TiAl, α_2-Ti_3Al and Ti_5Si_3, respectively, were obtained for the sample deformed at 1200 °C/0.1 s^{-1}. The weak textural intensity in the former sample was attributed to the high rate of DRX as evidenced by the highest efficiency of power dissipation at the deformed parameters (Fig. 8). This in turn, hindered the growth of the recrystallized grains into a preferred orientation. These results compare perfectly with the findings of Lavasani et al., [63]. The researchers obtained weak overall maximum textural intensities of 1.778 and 1.833 times stronger than a random distribution for the cast + homogenised Ti-48Al-2Cr samples compressed at 1000 °C/0.01 s^{-1} and 1000 °C/0.001 s^{-1}, respectively. However, the maximum intensity increased to 3.057 when the speed of compression was increased to 0.1 s^{-1}.

The boundary misorientation distribution profiles of the main phases (i.e. γ-TiAl and α_2-Ti_3Al) in the samples deformed at 1050 °C/0.01 s^{-1} and 1200 °C/0.1 s^{-1} are depicted in Fig. 14. It is apparent that for both sets of deformation parameters, boundaries with misorientations greater than 15° were predominant for both γ (Fig. 14a, b) and α_2 (Fig. 14c, d) phases. However, the distributions for α_2 phase indicate the presence of a significant number of boundaries with misorientations less than 15°. In general, the results demonstrate that the sample deformed at 1050

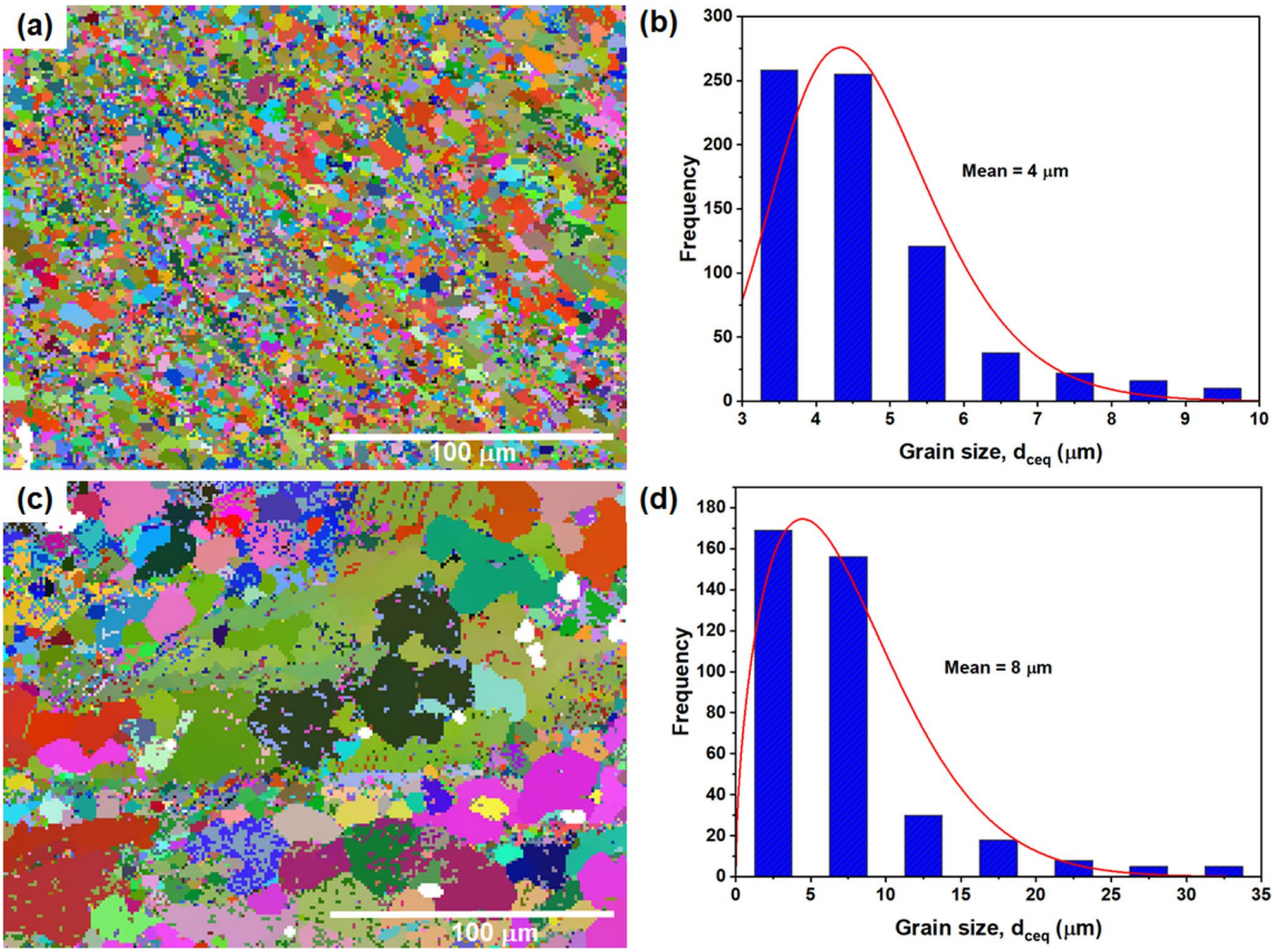

Fig. 12 Grain size analysis by EBSD. (**a**) and (**c**) all Euler colour maps, (**b**) and (**d**) histograms of equivalent circle diameter grain size distribution of the samples deformed at 1050 °C/0.01 s^{-1} and 1200 °C/0.1 s^{-1}, respectively

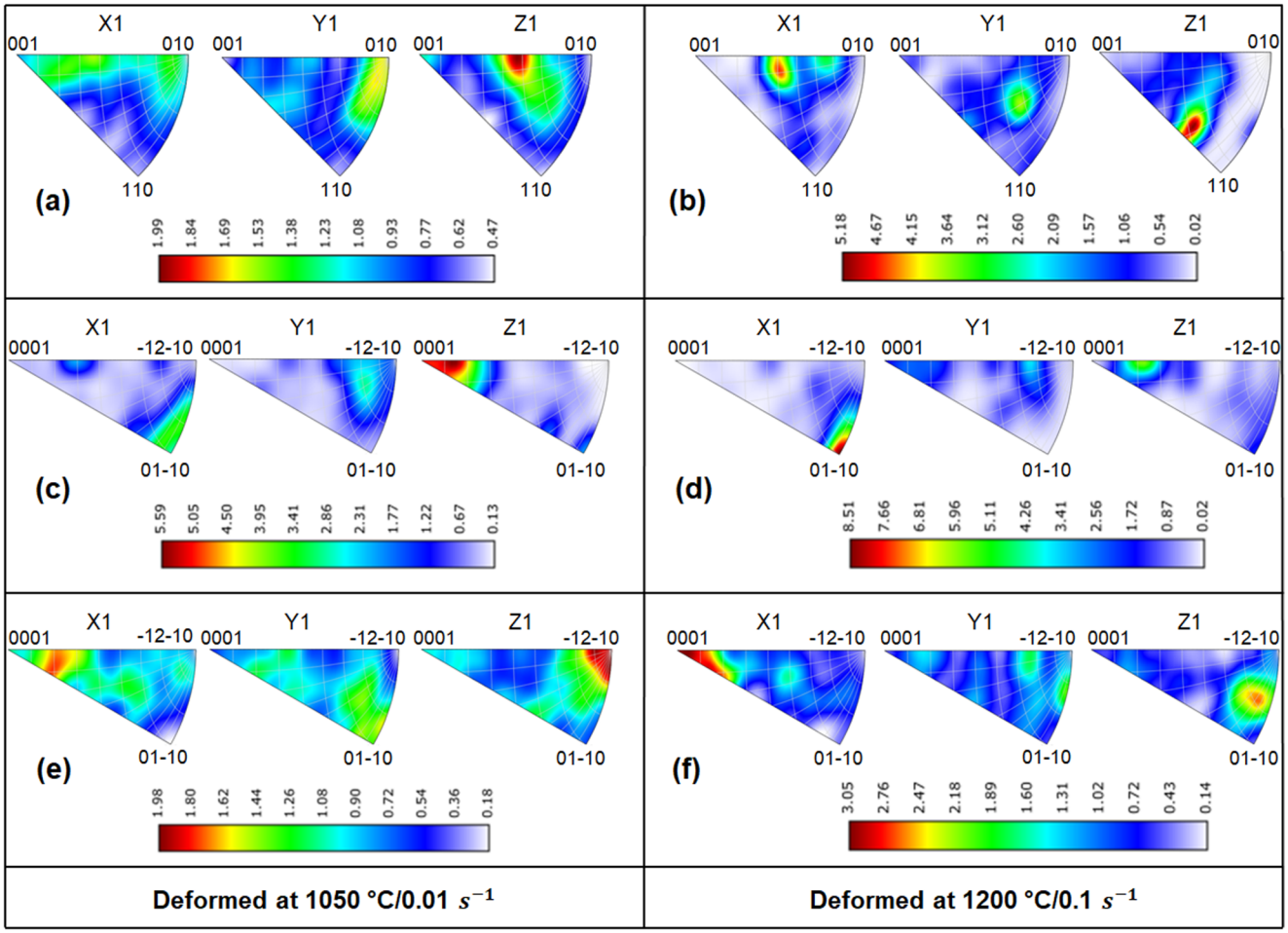

Fig. 13 ?111? inverse pole figures for (**a**), (**b**) γ-TiAl, (**c**), (**d**)α_2-Ti_3Al, and (**e**), (f) Ti_5Si_3

°C/0.01 s^{-1} consisted of about 91.4% high-angle grain boundaries (HAGBs) and 8.64% low-angle grain boundaries (LAGBs). Nevertheless, when the material was deformed at 1200 °C/0.1 s^{-1}, the HAGBs reduced to 82.5% whereas the LAGBs increased to 17.5%. According to the findings of Wu et al., [64] on the influence of grain boundaries on the mechanical properties of materials, it may imply that the sample deformed at 1050 °C/0.01 s^{-1} possessed better mechanical properties at room temperature than the one deformed at 1200 °C/0.1 s^{-1}.

Figure 15 displays the EBSD analysis of elastic properties (i.e. Young's modulus (E) and Shear modulus (G)) for specimens deformed at 1050 °C/0.01 s^{-1} (Fig. 15a) and 1200 °C/0.1 s^{-1} (Fig. 15b). The elastic property value for each main phase in each sample is exhibited in Fig. 15c as an average. As can be seen, the maximum value of the elastic properties in both samples was 222.65 GPa. However, the mean value of E for γ phase in the sample deformed at 1050 °C/0.01 s^{-1} was 190.61 GPa while for α_2 phase was 154.78 GPa. On the other hand, for the specimen deformed at 1200 °C/0.1 s^{-1}, the values for E were 181.97 and 159.02 GPa for γ and α_2 phases, respectively. In terms of values for G, γ phase in the sample deformed 1050 °C/0.01 s^{-1} possessed 74.05 GPa whereas α_2 phase possessed 62.65 GPa. Conversely, in the sample deformed at 1200 °C/0.1 s^{-1}, the values for G were 71.16 and 61.66 GPa for γ and α_2 phases, respectively. Therefore, one could deduce that the sample deformed at 1050 °C/0.01 s^{-1} possessed improved elastic properties compared to the one deformed at 1200 °C/0.1 s^{-1}. Table 6 shows a comparison of the elastic properties of the alloy deformed at 1050 °C/0.01 s^{-1} studied in this work with the previously published results. It is evident that the alloy investigated here possesses superior properties.

The geometrically necessary dislocation (GND) density analysis results for the samples deformed at 1050 °C/0.01 s^{-1} and 1200 °C/0.1 s^{-1} are presented in Fig. 16. The results were obtained using an approach referred to as the "Weighted Burgers Vector" (WBV) technique in AZtecCrystal viewing mode [69]. It can be observed that the sample deformed at 1050 °C/0.01 s^{-1} had a negligible level of dislocation

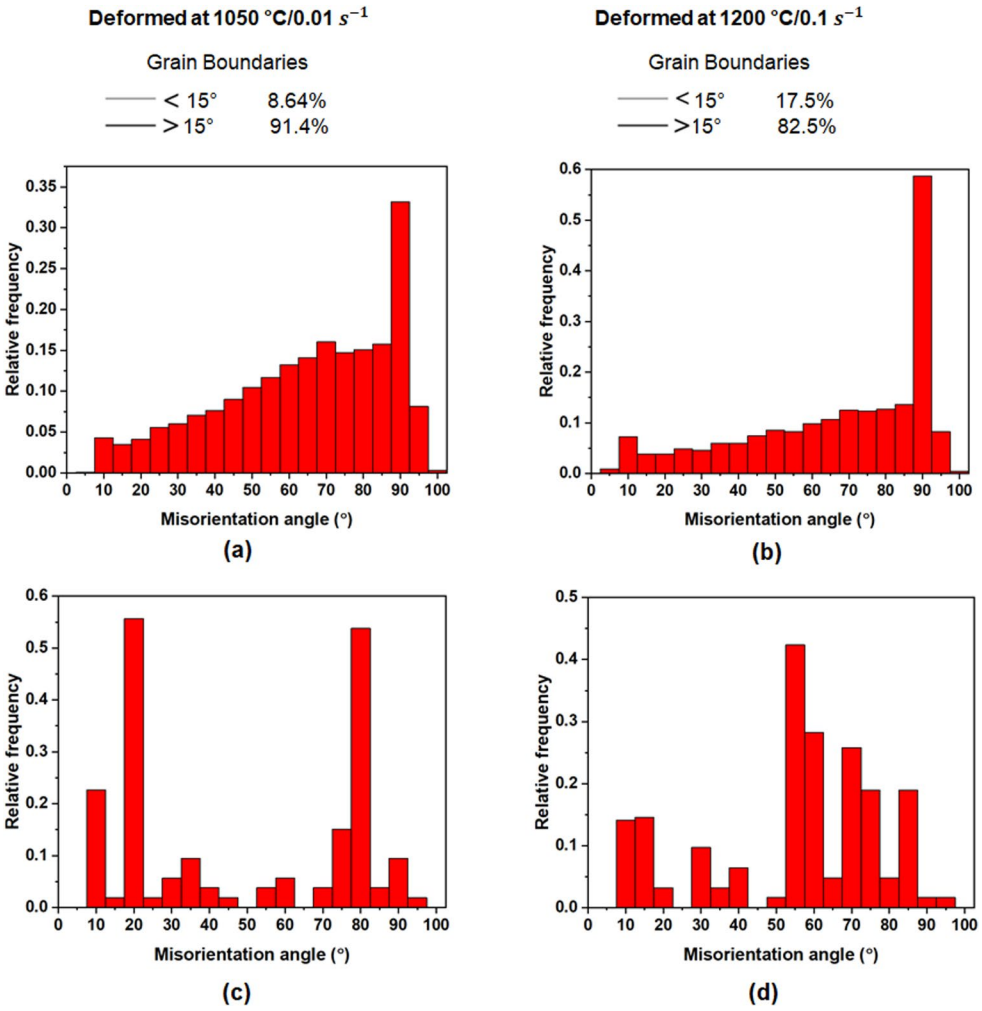

Fig. 14 Misorientation angle distribution of (**a**) and (**b**) γ (TiAl), (**c**) and (**d**) α_2 (Ti_3Al) for the samples deformed at 1050 °C/0.01 s^{-1} and 1200 °C/0.1 s^{-1}, respectively

density as evidenced by the vast area with a WBV magnitude of 0.00 μm^{-1} in the map (Fig. 16a). This may be attributed to the fact that the deformation parameters fall within the domain of high efficiency of power dissipation whereby the accumulation of dislocations during the hot compression had a maximum influence on DRX. On the contrary, the map for the sample deformed at 1200 °C/0.1 s^{-1} (Fig. 16b) exhibits large areas with a WBV magnitude range of about 0.02–0.06 μm^{-1} which signifies that the sample contained a significant level of dislocation density after hot compression.

4 Conclusion

The hot workability of a Si-doped modified second generation γ-TiAl alloy with a nominal composition of Ti-48Al-2Nb-0.7Cr-0.3Si (at%) fabricated from cold-pressed precursor powders through VAR and homogenization processes was investigated by the uniaxial thermal simulation compression tests in this work. The principal aims of the study were to characterize the alloy's response to hot deformation loading, to obtain the optimum hot-working windows and to analyze the as-deformed microstructures of the alloy deformed within the optimum hot-working domains. From the gathered results, the main conclusions drawn were as follows:

- The hot deformation of the alloy was chiefly characterized by a 45° shearing of the mid portion of the specimens to form macro-cracks which indicated a poor hot workability of the alloy at most of the deformation temperatures and strain rates.
- The flow curves showed that the flow stress decreased significantly with increasing temperature and decreasing strain rate. This signified that the alloy was a low stacking-fault-energy (SFE) material characterized

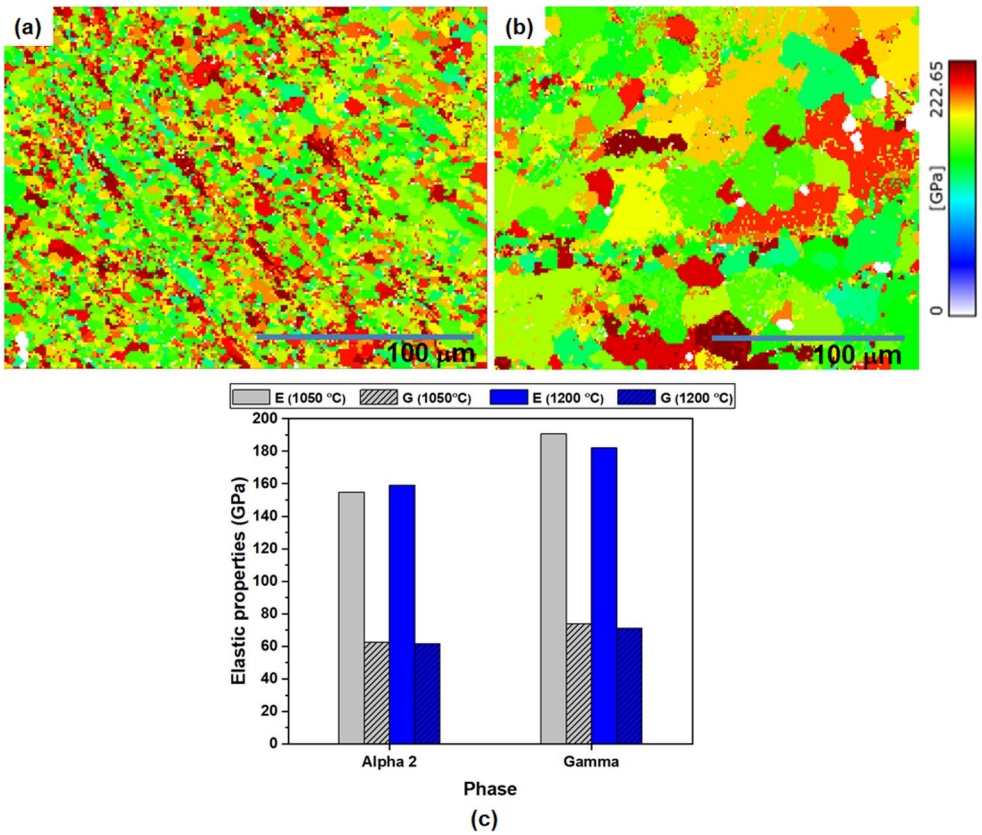

Fig. 15 (**a**) and (**b**) EBSD elastic property maps for samples deformed at 1050 °C/0.01 s^{-1} and 1200 °C/0.1 s^{-1}, respectively, (**c**) elastic properties of γ (TiAl) and α_2 (Ti_3Al) phases

Table 6 Elastic properties of γ-TiAl-based alloys

γ-TiAl alloy (at%)	Processing route	Young's modulus (GPa)	Shear modulus (GPa)	Ref.
Ti-42Al-8.5Nb	PM + HIP + Heat treatment (HT)	152	-	[65]
Ti-46.5Al-3Nb-2Cr-0.2 W	ISM + forging + HT	164	-	[66]
Ti-46Al-2.5Nb -3.2Cr	Centrifugal casting	154	-	[67]
Ti-46.5Al-4(Cr, Nb, Ta, B)	VAR	140	-	[68]
Ti-48Al-2Nb-0.7Cr-0.3Si	VAR + hot-compression	187	73	This study

mainly by the decreased mobility of dislocations during hot deformation.

- The activation energy for the alloy was 401 kJ/mol and the constitutive equation could be expressed as:

$$\dot{\epsilon} = 3.0528 \times 10^{13}[\sinh(0.0035\sigma_P)]^{4.3205}\exp\left(-\frac{401000}{RT}\right)$$

which exhibited a good linear correlation among flow stress, strain rate and temperature.

- An optimum hot working window for the alloy was identified to be within the temperature and strain rate ranges of about 1050–1080 °C and 0.0087–0.071s^{-1}, respectively.
- Although lamellae kinking was observed, DRX was the predominant softening mechanism during hot working at the optimum deformation conditions which resulted in nucleation of refined grains with a mean grain size of about 4 µm. Furthermore, the microstructure of the alloy at the optimum deformation parameters consisted of a high percentage of HAGBs, weak textural intensity and improved elastic properties with a negligible accumulation of remnant dislocations.

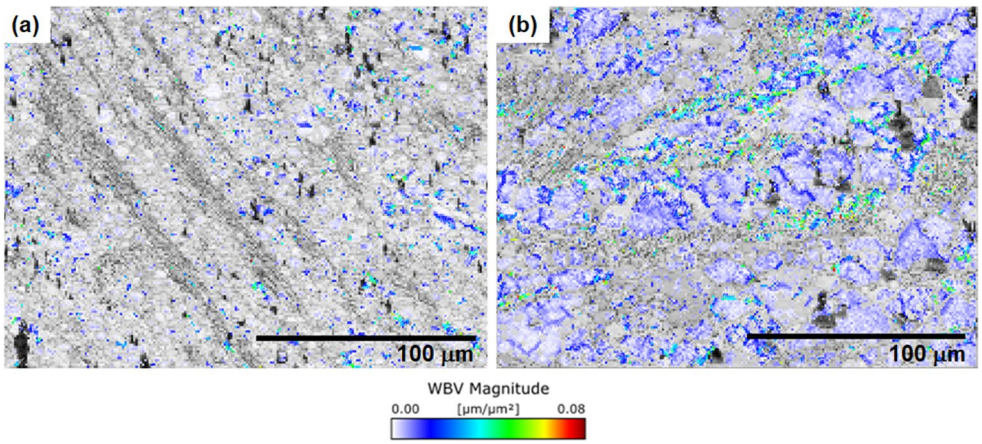

Fig. 16 EBSD dislocation density analysis maps of samples deformed at (**a**) 1050 °C/0.01 s^{-1}, and (**b**) 1200 °C/0.1 s^{-1}

Supplementary Information The online version contains supplementary material available at https://doi.org/10.1007/s00170-026-17834-y.

Acknowledgements The authors would like to acknowledge the University of Pretoria (UP) in the Republic of South Africa for providing laboratory equipment's.

Author contributions JJM Ellard was responsible for the material preparation, data collection, and analysis. All authors contributed to the conceptualization and design of the experiments. JJM Ellard wrote the initial draft of the manuscript, and all co-authors contributed to the formal analysis and provided comments on previous versions. The final manuscript was reviewed and approved by all authors.

Funding Open access funding provided by University of the Witwatersrand. This work was supported by the National Research Foundation in South Africa under the Competitive Support Grant (Ref no: CSUR240508217931).

Declarations

Consent for publication All authors confirm their agreement to the authorship, have read and approved the manuscript, and consent to its submission and subsequent publication. The authors collectively guarantee that this work represents an original contribution and has not been previously published elsewhere.

Conflict of interest The authors declare no competing interest.

References

1. Ellard JJM, Mathabathe MN, Siyasiya CW (2023) Bolokang. Low-Cycle Fatigue Behaviour of Titanium-Aluminium-Based Intermetallic Alloys: A Short Review. Met (Basel) 13(8):1491. https://doi.org/10.3390/met13081491
2. Lütjering G, Williams JC (2007) Titanium. Springer Berlin, Heidelberg XII, 442. https://doi.org/10.1007/978-3-540-73036-1
3. Appel F, Paul JDH, Oehring M (2011) Gamma Titanium Aluminide Alloys. Wiley. https://doi.org/10.1002/9783527636204
4. Erdely P, Werner R, Schwaighofer E, Clemens H, Mayer S (2015) In-situ study of the time–temperature-transformation behaviour of a multi-phase intermetallic β-stabilised TiAl alloy. Intermetallics (Barking) 57:17–24. https://doi.org/10.1016/j.intermet.2014.09.011
5. Genc O, Unal R (2022) Development of gamma titanium aluminide (γ-TiAl) alloys: A review. J Alloys Compd 929:167262. https://doi.org/10.1016/j.jallcom.2022.167262
6. Kim JH, Chang YW, Lee CS, Kwon T, Ha (2003) High-temperature deformation behavior of a gamma TiAl alloy—Microstructural evolution and mechanisms. Metall Mater Trans A 34(10):2165–2176. https://doi.org/10.1007/s11661-003-0280-0
7. Clemens H, Mayer S, Design (2013) Processing, Microstructure, Properties, and Applications of Advanced Intermetallic TiAl Alloys. Adv Eng Mater 15(4):191–215. https://doi.org/10.1002/adem.201200231
8. Appel F, Clemens H, Fischer FD (2016) Modeling concepts for intermetallic titanium aluminides. Prog Mater Sci 81:55–124. https://doi.org/10.1016/j.pmatsci.2016.01.001
9. Schwaighofer E et al (2014) Microstructural design and mechanical properties of a cast and heat-treated intermetallic multi-phase γ-TiAl based alloy. Intermetallics (Barking) 44:128–140. https://doi.org/10.1016/j.intermet.2013.09.010
10. Zhang W, Liu Y, Li HZ, Li Z, Wang H, Liu B (2009) Constitutive modeling and processing map for elevated temperature flow behaviors of a powder metallurgy titanium aluminide alloy. J Mater Process Technol 209(12–13):5363–5370. https://doi.org/10.1016/j.jmatprotec.2009.04.006
11. Huang J et al (2007) Simulation of hot compression of Ti–Al alloy. Intermetallics (Barking) 15(5–6):700–705. https://doi.org/10.1016/j.intermet.2006.10.019
12. Rao KP, Prasad YVRK, Suresh K (2011) Hot working behavior and processing map of a γ-TiAl alloy synthesized by powder metallurgy. Mater Des 32(10):4874–4881. https://doi.org/10.1016/j.matdes.2011.06.003

13. Bibhanshu N, Suwas S (2018) Hot Deformation and Dynamic Recrystallization in Titanium Aluminide. Mater Sci Forum 941:1391–1396. 10.4028/. www.scientific.net/MSF.941.1391
14. Tian S, Jiang H, Guo W, Zhang G, Zeng S (2019) Hot deformation and dynamic recrystallization behavior of TiAl-based alloy. Intermetallics (Barking) 112:106521. https://doi.org/10.1016/j.intermet.2019.106521
15. Singh V, Kumar A, Mondal C, Bhattacharjee PP, Ghosal P (2019) Hot deformation of high-Nb-containing γ-TiAl alloy in the temperature range of 1000–1200°C: microstructural attributes to hot workability. SN Appl Sci 1(4):366. https://doi.org/10.1007/s42452-019-0380-0
16. Schwaighofer E, Clemens H, Lindemann J, Stark A, Mayer S (2014) Hot-working behavior of an advanced intermetallic multi-phase γ-TiAl based alloy. Mater Sci Engineering: A 614:297–310. https://doi.org/10.1016/j.msea.2014.07.040
17. Gupta RK, Kumar VA, Raj JN, Singh BK (2021) Kanjarla. Hot Deformation Studies on β0 Stabilized TiAl Alloy Made Through Ingot Metallurgy Route. Trans Indian Inst Met 74(12):2977–2989. https://doi.org/10.1007/s12666-021-02366-8
18. Chen X et al (2021) Dynamic recrystallization and hot processing map of Ti-48Al-2Cr-2Nb alloy during the hot deformation. Mater Charact 179:111332. https://doi.org/10.1016/j.matchar.2021.111332
19. Hu Q, Wang Y, Lv L, Luo Y, Su L, Liu B (2023) Hot deformation behavior and dynamic recrystallization mechanism of Ti-48Al-2Nb-2Cr alloy with near-γ microstructure. J Alloys Compd 945:169378. https://doi.org/10.1016/j.jallcom.2023.169378
20. Ellard J, Mathabathe MN, Siyasiya C, Bolokang S (2022) Powder Characteristics blending and microstructural analysis of a hot-pack rolled vacuum arc-melted gamma-TiAl based sheet. S Afr J Ind Eng 32(3). https://doi.org/10.7166/33-3-2809
21. Mathabathe MN, Bolokang AS, Govender G, Mostert RJ (2018) Siyasiya. The vacuum melted ɣ-TiAl (Nb, Cr, Si)-doped alloys and their cyclic oxidation properties. Vacuum 154:82–89. https://doi.org/10.1016/j.vacuum.2018.04.055
22. Mathabathe MN, Bolokang AS, Govender G, Mostert RJ (2018) Siyasiya. The vacuum melted ɣ-TiAl (Nb, Cr, Si)-doped alloys and their cyclic oxidation properties. Vacuum 154(May):82–89. https://doi.org/10.1016/j.vacuum.2018.04.055
23. Dudziak T et al (2022) Scale mass gain, morphology and phase composition of air and steam oxidized electron beam melted and cast Ti–48Al–2Nb-0.7Cr-0.3Si alloys. Intermetallics (Barking) 145:107553. https://doi.org/10.1016/j.intermet.2022.107553
24. Processing Maps (2013) A Status Report. J Mater Eng Perform 22(10):2867–2874. https://doi.org/10.1007/s11665-013-0732-7
25. Prasad YVRK, Seshacharyulu T (1998) Modelling of hot deformation for microstructural control. Int Mater Rev 43(6):243–258. https://doi.org/10.1179/imr.1998.43.6.243
26. Ellard JJM, Mathabathe MN, Siyasiya C, Bolokang AS (2023) Vacuum melting of compressed powders and hot rolling of the as-cast Ti-48Al-2Nb-0.7Cr-0.3Si intermetallic alloy: Mechanical properties and microstructural analysis. J Manuf Process 101:1214–1223. https://doi.org/10.1016/j.jmapro.2023.06.060
27. Mathabathe MN, Bolokang AS, Govender G, Siyasiya CW, Mostert RJ (2019) Cold-pressing and vacuum arc melting of γ-TiAl based alloys. Adv Powder Technol 30(12):2925–2939. https://doi.org/10.1016/j.apt.2019.08.038
28. Magogodi S, Mathabathe M, Bolokang A, Siyasiya C (2022) The electrochemical corrosion behaviour of Ti-48Al-2Nb-0.7Cr-0.3Si alloy in 3.5%NaCl. MATEC Web Conferences 370:06008. https://doi.org/10.1051/matecconf/202237006008
29. Appel F, Brossmann U, Christoph U (2000) Eggert. Recent Progress in the Development of Gamma Titanium Aluminide Alloys. Adv Eng Mater 2:699–720
30. Rao KP (2010) Prasad. Processing map and hot working mechanisms in a P/M TiAl alloy composite with in situ carbide and silicide dispersions. Mater Sci Engineering: A 527(24–25):6589–6595. https://doi.org/10.1016/j.msea.2010.06.064
31. Prasad YVRK (2013) Processing maps: A status report. J Mater Eng Perform 22(10):2867–2874. https://doi.org/10.1007/s11665-013-0732-7
32. Prasad YVRK, Seshacharyulu T (2013) Modelling of hot deformation for microstructural control. Int Mater Rev 43(6):243–258. https://doi.org/10.1179/imr.1998.43.6.243
33. Mathabathe MN, Bolokang AS, Govender G, Mostert RJ, Siyasiya CW (2018) Structure-property orientation relationship of a γ/α2/Ti5Si3 in as-cast Ti-45Al-2Nb-0.7Cr-0.3Si intermetallic alloy. J Alloys Compd 765:690–699. https://doi.org/10.1016/j.jallcom.2018.06.265
34. Ellard JJM, Mathabathe MN, Siyasiya C, Bolokang AS (2023) Vacuum melting of compressed powders and hot rolling of the as-cast Ti-48Al-2Nb-0.7Cr-0.3Si intermetallic alloy: Mechanical properties and microstructural analysis. J Manuf Process 101(April):1214–1223. https://doi.org/10.1016/j.jmapro.2023.06.060
35. Fröbel U, Stark A (2015) Microstructural Evolution in Gamma Titanium Aluminides During Severe Hot-Working. Metall Mater Trans A 46(1):439–455. https://doi.org/10.1007/s11661-014-2607-4
36. Liu B, Liu Y, Li YP, Zhang W, Chiba A (2011) Thermomechanical characterization of β-stabilized Ti–45Al–7Nb–0.4 W–0.15B alloy. Intermetallics (Barking) 19(8):1184–1190. https://doi.org/10.1016/j.intermet.2011.03.021
37. Zhu L et al (2020) Dynamic recrystallization and phase transformation behavior of a wrought β-γ TiAl alloy during hot compression. Progress Nat Science: Mater Int 30(4):517–525. https://doi.org/10.1016/j.pnsc.2020.08.008
38. Zener C (1944) Hollomon. Effect of Strain Rate Upon Plastic Flow of Steel. J Appl Phys 15(1):22–32. https://doi.org/10.1063/1.1707363
39. Siyasiya CW (2015) Stumpf. Constitutive Constants for Hot Working of Steels: The Critical Strain for Dynamic Recrystallisation in C-Mn Steels. J Mater Eng Perform 24(1):468–476. https://doi.org/10.1007/s11665-014-1267-2
40. Sellars CM, McTegart WJ (1966) On the mechanism of hot deformation. Acta Metall 14(9):1136–1138. https://doi.org/10.1016/0001-6160(66)90207-0
41. Mirzadeh H (2019) Developing constitutive equations of flow stress for hot deformation of AZ31 magnesium alloy under compression, torsion, and tension. IntJ Mater Form 12(4):643–648. https://doi.org/10.1007/s12289-018-1440-5
42. Ge G, Zhang L, Xin J, Lin J, Aindow M, Zhang L (2018) Constitutive modeling of high temperature flow behavior in a Ti-45Al-8Nb-2Cr-2Mn-0.2Y alloy. Sci Rep 8(1):5453. https://doi.org/10.1038/s41598-018-23617-7
43. Sprengel W, Oikawa N, Nakajima H (1996) Single-phase interdiffusion in TiAl. Intermetallics (Barking) 4(3):185–189. https://doi.org/10.1016/0966-9795(94)00033-6
44. Herzig C, Przeorski T, Mishin Y (1999) Self-diffusion in γ-TiAl: an experimental study and atomistic calculations. Intermetallics (Barking) 7(3–4):389–404. https://doi.org/10.1016/S0966-9795(98)00117-4
45. Ellard JJM et al (2025) Engineering γ-TiAl alloys: The effects of Sn, Si and Mn on densification, microstructure, and mechanical properties. Intermetallics (Barking) 181:108746
46. Wang G, Xu L, Tian Y, Zheng Z, Cui Y, Yang R (2011) Flow behavior and microstructure evolution of a P/M TiAl alloy during high temperature deformation. Mater Sci Engineering: A 528(22–23):6754–6763. https://doi.org/10.1016/j.msea.2011.05.071

47. Gupta RK, Narayana Murty SVS, Pant B, Agarwala V, Sinha PP (2012) Hot workability of γ + α2 titanium aluminide: Development of processing map and constitutive equations. Mater Sci Engineering: A 551:169–186. https://doi.org/10.1016/j.msea.2012.05.005
48. Chen Y, Yang F, Kong F (2011) Constitution modeling and deformation behavior of yttrium bearing TiAl alloy. J Rare Earths 29(2):114–118. https://doi.org/10.1016/S1002-0721(10)60414-0
49. Bartels A, Kestler H, Clemens H (2002) Deformation behavior of differently processed γ-titanium aluminides. Mater Sci Engineering: A 329–331:153–162. https://doi.org/10.1016/S0921-5093(01)01552-0
50. Semiatin SL, Cornish GR, Eylon D (1994) Hot-compression behavior and microstructure evolution of pre-alloyed powder compacts of a near-γ titanium aluminide alloy. Mater Sci Eng: A 185(1–2):45–53. https://doi.org/10.1016/0921-5093(94)90926-1
51. Liu ZC, Lin JP, Wang YL, Lin Z, Chen GL (2004) Chang. High temperature deformation behaviour of As-cast Ti–46Al–8.5Nb–0.2 W alloy. Mater Lett 58(6):948–952. https://doi.org/10.1016/j.matlet.2003.07.049
52. Liu B, Liu Y, Zhang W, Huang JS (2011) Hot deformation behavior of TiAl alloys prepared by blended elemental powders. Intermetallics (Barking) 19(2):154–159. https://doi.org/10.1016/j.intermet.2010.08.024
53. Jiang H, Zeng S, Zhao A, Ding X, Dong P (2016) Hot deformation behavior of β phase containing γ-TiAl alloy. Mater Sci Engineering: A 661:160–167. https://doi.org/10.1016/j.msea.2016.03.005
54. Li J, Liu Y, Wang Y, Liu B, He Y (2014) Dynamic recrystallization behavior of an as-cast TiAl alloy during hot compression. Mater Charact 97:169–177. https://doi.org/10.1016/j.matchar.2014.09.013
55. Kong FT, Chen YY, Li BH (2009) Influence of yttrium on the high temperature deformability of TiAl alloys. Mater Sci Engineering: A 499(1–2):53–57. https://doi.org/10.1016/j.msea.2007.09.093
56. Singh V, Mondal C, Kumar A, Bhattacharjee PP, Ghosal P (2019) High temperature compressive flow behavior and associated microstructural development in a β-stabilized high Nb-containing γ-TiAl based alloy. J Alloys Compd 788:573–585. https://doi.org/10.1016/j.jallcom.2019.02.207
57. Schwaighofer E, Clemens H, Lindemann J, Stark A, Mayer S (2014) Hot-working behavior of an advanced intermetallic multi-phase γ-TiAl based alloy. Mater Sci Eng A 614:297–310. https://doi.org/10.1016/j.msea.2014.07.040
58. Chen X et al (2021) Dynamic recrystallization and hot processing map of Ti-48Al-2Cr-2Nb alloy during the hot deformation. Mater Charact 179(127):111332. https://doi.org/10.1016/j.matchar.2021.111332
59. Kahrobaee Z, Palm M (2022) Experimental investigation of Ti–Al–Si phase equilibria at 800–1200°C. J Alloys Compd 924:166223. https://doi.org/10.1016/j.jallcom.2022.166223
60. Luo R et al (2021) Characteristic and mechanism of dynamic recrystallization in a newly developed Fe-Cr-Ni-Al-Nb superalloy during hot deformation. J Alloys Compd 865:158601. https://doi.org/10.1016/j.jallcom.2021.158601
61. Tian S, Jiang H, Guo W, Zhang G, Zeng S (2019) Hot deformation and dynamic recrystallization behavior of TiAl-based alloy. Intermetallics (Barking) 112(May):106521. https://doi.org/10.1016/j.intermet.2019.106521
62. Sun FS (2002) Froes. Precipitation of Ti5Si3 phase in TiAl alloys. Mater Sci Eng A 328(1):113–121. https://doi.org/10.1016/S0921-5093(01)01678-1
63. Navaei N, Reza H, Arabi H, Park N (2018) Materials science & engineering a texture analysis and development of ultra fi ne grained structure during thermo-mechanical treatment in a gamma-TiAl intermetallic. Mater Sci Eng A 711(November 2017):259–267. https://doi.org/10.1016/j.msea.2017.11.023
64. Wu H, Cong J, Liu Q, Zhao J, Wang Z, Wang X (2023) Research on influence of grain boundaries on the mechanical properties of 460 MPa refractory steel used for high-strength building structures. Mater Res Express 10:076510. https://doi.org/10.1088/2053-1591/ace29b
65. Janovská M, Rackel MW, Pyczak F, Stark A (2023) Impact of microstructure on elastic properties in the alloy Ti-42Al-8.5 Nb. J Alloys Compd 932:167578. https://doi.org/10.1016/j.jallcom.2022.167578
66. Iii WJP, John R, Olson S (2003) Determination of Young Õ s modulus of grains in a gamma titanium aluminide alloy. 49:327–332. https://doi.org/10.1016/S1359-6462(03)00280-X
67. Pilone D et al (2020) Mechanical behaviour of an Al2O3 Dispersion Strengthened γTiAl Alloy Produced by Centrifugal casting. Metals 10(11):1457. https://doi.org/10.3390/met10111457
68. Ma T, Chen R, Zheng D, Liu C, Guo J, Ding H (2017) Hydrogenation behavior of Ti – 44Al – 6Nb alloy and its effect on the microstructure and hot deformability. https://doi.org/10.1557/jmr.2016.520
69. Trimby P, Drury MR (2009) The weighted Burgers vector: a new quantity for constraining dislocation densities and types using electron backscatter diffraction on 2D sections through crystalline materials. 233(December 2008):482–494. https://doi.org/10.1111/j.1365-2818.2009.03136.x